To link to this article: DOI:10.1002/fld.2613

http://dx.doi.org/10.1002/fld.2613

On the relative impact of subgrid-scale modelling and conjugate heat transfer in LES of hot jets in cross-flow over cold plates

Y. Hallez [1,*,†], J.-C. Jouhaud [1] and T. J. Poinsot [2]

[1] *CERFACS, 42 Avenue Gaspard Coriolis, 31057 Toulouse Cedex 01, France*
[2] *IMFT (UMR CNRS-INPT-UPS 5502), Toulouse, France*

SUMMARY

This work describes numerical simulations of a hot jet in cross-flow with applications to anti-ice systems of aircraft engine nacelles. Numerical results are compared with experimental measurements obtained at ONERA to evaluate the performances of LES in this industrial context. The combination of complex geometries requiring unstructured meshes and high Reynolds number does not allow the resolution of boundary layers so that wall models must be employed. In this framework, the relative influence of subgrid-scale modelling and conjugate heat transfer in LESs of aerothermal flows is evaluated. After a general overview of the transverse jet simulation results, a LES coupled with a heat transfer solver in the walls is used to show that thermal boundary conditions at the wall have more influence on the results than subgrid scale models. Coupling fluid flow and heat transfer in solids simulations is the only method to specify their respective thermal boundary conditions.

KEY WORDS: fluid-structure coupling; conjugate heat transfer; large eddy simulation; hot jet in cross-flow; subgrid-scale modelling; transverse jet

1. INTRODUCTION

Aerothermal flows are ubiquitous in industrial applications especially in aeronautics. Some examples are cooling jets along the blades of gas turbines or anti-ice systems on planes, which are both related to the canonical problem of a jet in cross-flow (JCF). To solve this problem numerically, (Unsteady-) Reynolds Averaged Navier–Stokes (RANS) simulations were conducted and it was shown that simple two-equation models such as the standard $k-\epsilon$ model were able to predict the gross flow field, but did not reproduce well the average lateral jet width and the average jet's penetration in the cross-flow [1, 2]. Turbulent statistics also seem difficult to predict with these methods. Because certain parts of the flow are strongly anisotropic, Reynolds Stress Models were expected to be more accurate but they were not found to do especially better than two-equation models [1]. This may be linked to the need to resolve the temporal behaviour of the jet or to find closures for the pressure–velocity and triple velocity correlations satisfactory for both in a jet regime and in a boundary layer regime. Because computer power is continuously increasing, it is now conceivable to use LESs, which do not suffer from these problems of flexibility, to study some of these complex flows. In comparison to RANS simulations, LES have provided better agreement with experimental data (e.g. [3–5]). During the last two decades, the subgrid-scale (SGS) models used in these LES have considerably evolved since Smagorinsky's pioneering work [6]. Almost every new model has shown improvements over previous ones when tested in academic simulations. However, it is more

*Correspondence to: Y. Hallez, LGC, UPS bât. 2R1, 118 route de Narbonne, 31062 Toulouse Cedex 9, France.
†E-mail: hallez@chimie.ups-tlse.fr

difficult to assess the superiority of a given model in simulations involving complex geometries, unstructured meshes and complex boundary conditions.

The aim of the present work is to compare the relative impacts of SGS modelling and wall thermal boundary conditions in a complex flow involving heat transfer, namely a hot JCF. An accurate thermal boundary condition for the fluid flow is proposed by coupling the fluid solver with a heat transfer solver in the walls. In the following, it is shown that the simulation using this 'ideal boundary condition' performs better than simulations with a classical adiabatic or isothermal wall boundary condition. An improvement of the SGS model from the Wall-Adapting Local Eddy-viscosity (WALE) model [7] to the Wall-adapting Similarity Mixed model (WSM) [8] is also evaluated.

An extensive literature exists concerning transverse jets with a high jet to cross-flow velocity ratio $R = W_j/U_\infty$ (typically $R > 2$), where W_j is the average vertical velocity at the jet exhaust and U_∞ is the free-stream cross-flow velocity. This is certainly linked to early military researches on this flow with applications on the reaction control of rockets and missiles, V/STOL aircraft or environmental concerns on plume dispersal from smoke stacks or volcanoes [9]. A few recent ones are those in [10–15], and a great number of others referenced therein. Studies involving JCF with a low velocity ratio ($R < 1$), are also numerous [16–22]. Recent studies on these low-R jets are generally motivated by the problem of surface warming or cooling encountered in applications such as turbine blades or combustion chamber walls cooling (e.g. [23] and references therein). Because relatively few studies of a single low-R high-Re square jet in cross-flow are available, a general overview of the flow obtained from a LES at $Re \simeq 10^5$ will be proposed in Section 4, after the problem setup and the numerical approach are described. Dynamical and thermal quantities will then be given for the different LES configurations. Finally, some conclusions will be drawn concerning the impact of the SGS model and of thermal boundary conditions on the solution quality.

2. FLOW DOMAIN AND BOUNDARY CONDITIONS

The aerothermal system studied here is inspired from the square hot JCF setup investigated experimentally in [24] and reproduced numerically in [2]. This is a rather geometrically complex setup because the experimental jet in the cross-flow device in [24] was mounted on a wing profile, which reproduced a (small) nacelle curvature on its extrado to remain close to their applications (Figure1). It has nonetheless been chosen to reproduce this setup in the present simulations, instead of a more canonical one that would have been sufficient for the present work, because of the extensive experimental data available in [24]: average and fluctuating velocities, average and fluctuating temperature in the fluid, and temperature of the solid wall. This last type of measurement is particularly useful to assess the quality of the numerical coupling between the aerothermal flow and the thermics in the wall.

The numerical domain used in the present work corresponds geometrically to the extrado of the device in [24] but assumes zero curvature, as depicted in Figure 2. A Cartesian basis $(\mathbf{e_x}, \mathbf{e_y}, \mathbf{e_z})$ is defined, where $\mathbf{e_x}$ is the streamwise 'cross-flow' direction and $\mathbf{e_y}$ is the spanwise direction. The hot jet exhausts through a hole of width $L = 0.03$ m pierced in a plane wall whose normal direction is $\mathbf{e_z}$ and whose location is $z = 0$. The hot fluid flowing through this hole comes from a scoop located

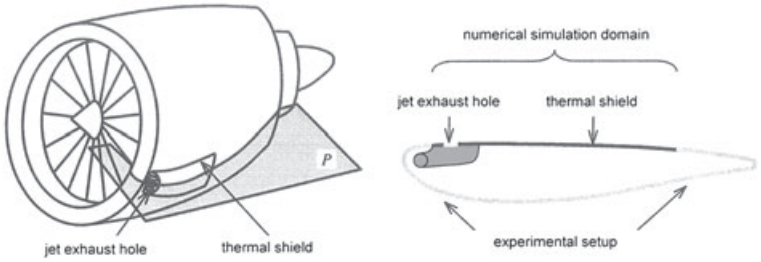

Figure 1. Adapted from [24]. Left: real application. Right: experimental setup in [24]. The numerical domain corresponds to the upper part of the experimental device and assumes a flat surface as depicted in Figure 2.

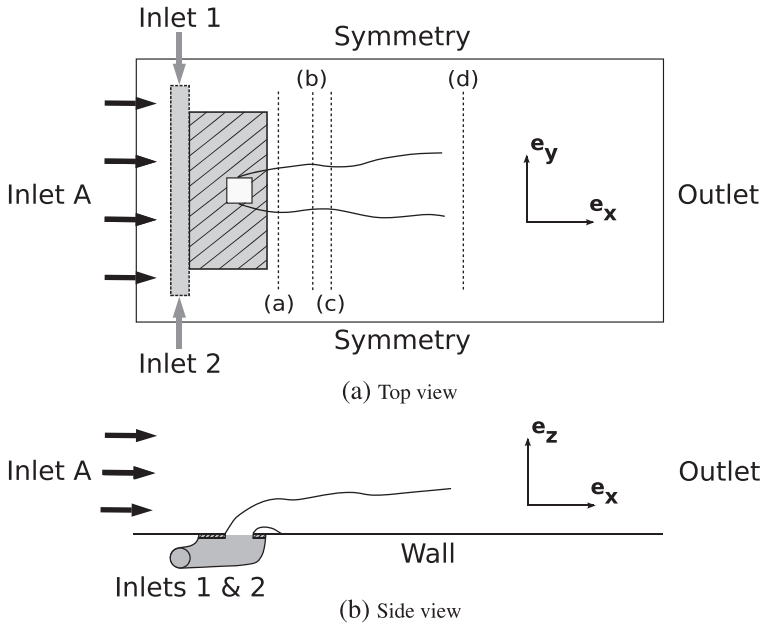

Figure 2. Sketch of the computational domain. The shaded zone is the scoop. The heat equation is solved within the scoop top wall marked with stripes. The (a), (b), (c) and (d) dashed lines indicate the positions of the measurements inside the jet at $x/L = 1$, $x/L = 2.3$, $x/L = 3$ and $x/L = 8$, respectively.

beneath the plane wall ($z < 0$), which collects fluid coming from two cylinders of axis $\mathbf{e_y}$ (denoted Inlet 1 and Inlet 2 in Figure 2). The scoop is included in the simulation because the external cross-flow is expected to affect the flow beneath the hole (e.g. [4, 13, 18]). The scoop hole is centered at $y = 0$, its downstream edge is located at $x = 0$, and its upstream side is at $x/L = -1$. The upper part of the scoop (striped zone on Figure 2) will be referred to as 'the scoop plate'.

An adiabatic wall law boundary condition is imposed on the wall around the scoop plate; symmetry conditions are imposed in the spanwise direction and a free slip boundary condition is prescribed on the plane at $z = z_{\max}$. On the scoop plate, a wall law is used and the type of thermal boundary condition to be imposed is discussed in this work. Besides, we impose the mean experimental velocity profile in [24] at the Inlet A, with a free-stream velocity $\mathbf{U}_\infty = U_\infty \mathbf{e_x}$ where $U_\infty = 47.4\,\mathrm{ms}^{-1}$. Because the experimental turbulence intensity is very low at this inlet (less than 1%), no turbulent fluctuations are injected in the simulation (a simulation with turbulence injected at the inlet, not presented here, showed no difference with the present simulations). Therefore, the only length scale in the flow is the size of the scoop hole L, and the Reynolds number is defined as $Re = U_\infty L/\nu \simeq 10^5$ where $\nu = 1.4\,10^{-5}\,\mathrm{m^2 s^{-1}}$ is the kinematic viscosity of air. Experimental velocity profiles are also imposed at inlets 1 and 2 in the scoop, with a maximum velocity of $53\,\mathrm{ms}^{-1}$.

In nonconstant density flows, the nondimensional group $R' = \sqrt{\rho_\mathrm{j}/\rho_\infty}(W_\mathrm{j}/U_\infty) = \sqrt{\rho_\mathrm{j}/\rho_\infty}R$ involving the momentum flux ratio is a better correlation parameter than R [9]. In the present work $\sqrt{\rho_\mathrm{j}/\rho_\infty} = 0.91$, $R' \simeq 0.78$ and $R \simeq 0.85$. The values of R and R' are similar because the Mach number is low ($M_\infty \simeq 0.14$) so that compressibility effects can be ignored, and the temperature variations do not exceed 60 K which permits to neglect thermal dilatation effects. Considering the closeness of R and R', keeping in mind that the geometry of the jet exhaust hole and the jet velocity profile may also have an influence on the flow, which is not taken into account in either R or R' [12], and because no atempt to build a correlation depending on R or R' is involved in the present work, the simple velocity ratio R will be used in the remainder of this article. The value of R is relatively low and corresponds to a jet attached to the wall downstream [18, 25]. The fluid is assumed to be air, the scoop grid has the properties of stainless steel and the downstream wall is adiabatic, as it is supposed to be in the experimental study in [24]. The corresponding physical parameters relative to the heat transfer problem are shown in Table I.

Table I. Physical parameters used in the present simulations.

	λ	ρ	c_p	$\mathcal{D}$	E
Air	0.0234	1.28	1005	$1.82\,10^{-5}$	5.5
Stainless steel	16	8000	500	410^{-6}	8000

λ, thermal conductivity ($\mathrm{Wm}^{-1}K^{-1}$); ρ, density ($\mathrm{kg\,m}^{-3}$); c_p, specific heat capacity ($\mathrm{J\,kg}^{-1}\mathrm{K}^{-1}$); $\mathcal{D}$, thermal diffusivity ($\mathrm{m}^2\mathrm{s}^{-1}$); E, Effusivity ($\mathrm{J\,m}^{-2}\mathrm{K}^{-1}$).

3. NUMERICAL SETUP

The compressible LES code AVBP [23, 26–28] were used to solve the fluid flow and the heat transfer problem inside the solid was addressed with the AVTP code [29, 30]. The numerical approaches and the physical modelling chosen for this work are shortly described in this section.

3.1. Numerical approach

The compressible Navier–Stokes equations are solved on an unstructured grid thanks to a cell-vertex finite volume/finite element approach. The convective terms are handled with a TTGC scheme [31], which belongs to the Two-step Taylor–Galerkin family [32] and is designed to minimize its numerical dissipation for a consistent use with LES. A small amount of second-order and fourth-order artificial dissipation is added to suppress spurious oscillations and it has been checked that the artificial viscosity level is always much smaller than the subgrid viscosity level. The mesh is constituted of $2.2\,10^6$ nodes and $12\,10^6$ cells and refined in the vicinity of the jet with a typical cell size of $L/20$. The position in terms of wall units of the first point off the wall has been measured a posteriori and is approximately 200, which is consistent with the use of a wall model. The mesh has been refined until the numerical results were close to the experimental ones in [24]. The zone requiring most refinement was located just downstream of the jet, typically for $0 < x/L < 2$. Symmetry of the mesh about the $y = 0$ plane had to be enforced so that the flow also remains statistically symmetrical about this plane.

The heat conduction solver AVTP uses the same data structure and the same numerical scheme for the diffusion term as AVBP to solve for the temperature field within the scoop top wall (marked with stripes on Figure 2). The size of the cells within the scoop plate is dictated by the need to discretize at least coarsely the solid domain in the z direction. The plate has a thickness of $L/18.75$ and five cells are used in this direction so that the uniform size cells in the solid plate have a length scale of roughly $L/100$. The whole scoop plate is constituted of approximately $3.4\,10^5$ nodes and $1.7\,10^6$ tetrahedra.

3.2. Subgrid-scale modelling

The Wall Adapting Local Eddy-viscosity model [7] (WALE) and the Wall-adapting Similarity Mixed model [8] (WSM) have been tested. The WALE model is an eddy-viscosity model based on the square of the velocity gradient tensor. It is able to produce the correct y^3 scaling for the SGS viscosity near a wall without requiring a dynamical procedure. However, this SGS viscosity is always positive which prevents any form of backscatter. Moreover this purely eddy-viscosity type of model also assumes that the SGS stress tensor is aligned with the resolved strain rate tensor, an hypothesis which is physically too restrictive. In order to remove this limitation and allow for backscatter, such eddy-viscosity models are often coupled with a scale-similarity model [33]. The WSM [8] is precisely issued from the coupling of the WALE eddy-viscosity model and the Bardina scale-similarity model, and should thus be expected to improve the simulation results particularly in jet flows where a strong correlation between the subgrid scale tensor and the Bardina model has been found in a priori tests [34]. Concerning the energy equation, an hypothesis of constant subgrid Prandtl number is used and $Pr^{\mathrm{SGS}} = 0.6$ has been chosen. One additional simulation with $Pr^{\mathrm{SGS}} = 0.3$ has been conducted to check the influence of this parameter.

3.3. Choice of thermal boundary conditions on the scoop

As the top plate of the scoop is thin, metallic and separates two flows with different temperatures, the choice of the boundary condition on it is not straightforward.

One first hypothesis would be to neglect heat transfer through this grid, compared with the heat transfer and mixing between the hot jet fluid and the cold exterior fluid. This is achieved by imposing an adiabatic boundary condition on the energy equation on both sides of the grid. In the present work, this approximation is used in the 'Adiab-WALE' simulation.

To obtain more accurate results, heat transfer between the scoop fluid and the exterior fluid through the top plate has to be taken into account. It is interesting to compare the characteristic time scales in the solid and in the fluid. The time scale associated to heat transfer through the plate from the scoop to the exterior is a diffusive one and can be expressed as

$$\mathcal{T}_\mathrm{s} = d^2/\mathcal{D}_\mathrm{s}, \tag{1}$$

where d is the plate thickness and $\mathcal{D}_\mathrm{s}$ is the thermal diffusivity in the solid plate. The exterior flow above the plate is dominated by advection and so a relevant fluid large time scale is

$$\mathcal{T}_f = L/U_\infty. \tag{2}$$

With these definitions, $\mathcal{T}_\mathrm{s}/\mathcal{T}_\mathrm{f} = (d/L)^2 PeA$, where $Pe = LU_\infty/\mathcal{D}_f$ is the Peclet number and $A = \mathcal{D}_\mathrm{f}/\mathcal{D}_\mathrm{s}$ is the ratio of thermal diffusivities. In most aeronautical applications $Pe \gg 1$ and $A \sim O(1)$, so that the solid time scale is always much greater than the larger time scale of the flow. As an example, the parameters in Table I lead to $\mathcal{T}_\mathrm{s}/\mathcal{T}_\mathrm{f} \simeq 10^3$. In other words, a temperature fluctuation will propagate much slower in the solid than in the fluid. Moreover, the very high ratio of the solid and fluid effusivities ($E_\mathrm{s}/E_\mathrm{f} \simeq 1450$) indicates that if a thermal fluctuation in the fluid encounters the plate, the latter will almost not change its temperature. These two behaviours are characteristic of most air/metal contacts, and support the approximation of imposing a steady temperature as a boundary condition for the fluid on the scoop plate.

The plate is, however, thermally driven by the heat transfer with the fluid, and its temperature is therefore not expected to be spatially uniform. It is necessary to compute either analytically or numerically the solution of the coupled heat transfer problem to know what the temperature profile is in the plate. This is actually rarely done and in most applications a spatially uniform temperature is imposed as a boundary condition when adiabatic conditions are not used. In the present work, such an approach is used for simulating 'IsoT-WALE' in which the plate temperature is enforced at $T_\mathrm{s} = (T_\mathrm{h} + T_\mathrm{c})/2$ for simplicity, where $T_\mathrm{h} = 363\,\mathrm{K}$ is the temperature of the hot air inside the scoop and $T_\mathrm{c} = 293\,\mathrm{K}$ is the temperature of the cold air in the cross-flow far from the jet.

Finally, a coupled simulation between LES and the scoop temperature field will be performed. It would be tempting to compute a full numerical solution of the conjugate heat transfer problem. However, the time scale needed to converge the solid problem is at least of order $H^2/\mathcal{D}_\mathrm{s} \sim O(10^4)\,\mathrm{s}$ (where $H \sim O(10L)$ is the largest dimension of the scoop plate) whereas the CFL condition in the fluid flow restricts the time step to $\mathrm{d}x/U_\infty \sim O(10^{-5})\,\mathrm{s}$, that is, at least 10^9 iterations would be needed even without resolving acoustic time scales. Hence, it is only possible to compute a stationary solution of the coupled problem. Fortunately, once the steady solution in the solid is obtained it is not expected to be much perturbed by the unsteady (zero-mean) thermal fluctuations in the fluid due to the nature of the materials used and the high-Re high-Pe flow. Because this work is focused essentially on the accuracy of the fluid flow solution, an unsteady LES simulation 'Ideal-WALE' is performed with the temperature obtained from the steady coupled problem imposed as a thermal boundary condition on the scoop plate. It should be emphasised that this LES simulation 'Ideal-WALE' is *not* a fully coupled one because it would be unaffordable, but it incorporates the best information available on the boundary condition thanks to the steady coupled simulation.

3.4. Computation of the steady state plate temperature

As mentioned above, the temperature inside the scoop plate is determined by heat transfer with the surrounding flow in a complex manner. Therefore, a coupled simulation has been set up to obtain

this field. The AVBP and AVTP codes were used to solve the fluid flow and the solid temperature field, respectively. The organisation of the communications between these two codes was handled thanks to the open source PALM library [35, 36]. Because of the large separation between the fluid time scale $\mathcal{T}_\mathrm{f}$ and the solid time scale $\mathcal{T}_\mathrm{s}$, a stationary solution is sought in the solid. Hence, it is not necessary for the fluid and solid simulations to be synchronised in time, and the fluid solver can advance n_f iterations representing a physical time τ_f while the solid solver advances n_s iterations representing a time τ_s before the coupling exchanges are made. This desynchronisation makes it possible for the solid solver to reach time scales as big as $\mathcal{T}_\mathrm{s}$ while the fluid solver reaches only much smaller time scales. Further details on this procedure are given in [30].

The temperature field obtained with this numerical coupling strategy is now presented in terms of thermal efficiency η defined by

$$\eta = \frac{T - T_\mathrm{c}}{T_\mathrm{j} - T_\mathrm{c}}, \tag{3}$$

where T is the local temperature, T_c is the cold cross-flow temperature and T_j is the average jet temperature in the scoop hole. The isothermal boundary condition $T = (T_\mathrm{c} + T_\mathrm{h})/2$ corresponds to a uniform efficiency $\eta \simeq 0.58$. The temperature field within the solid at the upper surface of the scoop plate obtained from the steady coupled simulation is presented in Figure 3. It is quite close to the isothermal boundary condition tested in the present work, but with an average temperature slightly lower. Moreover, downstream of the jet, the real temperature is actually higher than the average temperature because of the warming of the hot jet on the upper surface of the plate. Upstream of the jet, the incoming cross-flow cold fluid is warmed progressively as it travels in the x direction above the plate. A thermal boundary layer is thus developing from $x/L = -2.3$. Because this boundary layer is growing in the x direction, the scoop plate is more and more shielded from the cold cross-flow air as x/L progresses from -2.3 to 0.3. Therefore, a streamwise temperature gradient is observed in the solid plate, as seen for $y/L = \pm 3$ in Figure 3. Upstream of the jet, the flow is decelerated, which enables the cross-flow fluid to be more warmed by the plate around $y/L = 0$. This temperature field will be imposed to the fluid flow as a Dirichlet boundary condition in the Ideal-WALE simulation.

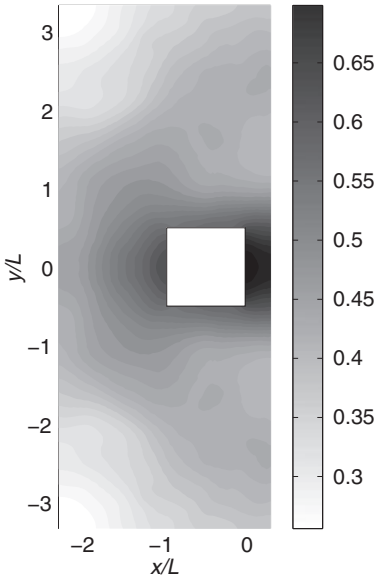

Figure 3. Thermal efficiency (see Equation (3)) in the solid at the upper surface of the scoop plate as computed with the steady coupled simulations. The isothermal boundary condition $T = (T_\mathrm{c} + T_\mathrm{h})/2$ would provide a uniform efficiency $\eta \simeq 0.58$.

Before the details of the simulation results are given, a brief overview of the flow computed numerically is presented and the general organization of the flow is compared to the observations available in the literature.

4. GENERAL OVERVIEW OF THE FLOW

Three main regimes of JCF exist according to the value of the jet to cross-flow velocity ratio R [22,25]. For large values of R (typically $R \geqslant 2$) the jet is said to be 'lifted' from the wall. For $R \leqslant 1$ it is 'attached' to the wall. For intermediate values it may be called 'reattached'. These particular values of R have been cited for circular jets, but depend slightly on the exhaust hole geometry [22]. In the present work, $R = 0.85$ and a square hole is considered. According to the general picture of the flow given in Figures 4 and 5, the present jet is in the attached or reattached regime. The simulation setup used for the description of the flow field provided in this section is the IsoT-WALE one. The features presented here are, however, identical for all the boundary conditions and SGS modelling tested.

The general average structure of the flow can be depicted in Figures 5 and 6. It is recalled that the square hole is located at $z = 0$, $-1 < x/L < 0$ and $-0.5 < y/L < 0.5$. The streamlines of the mean two-dimensional flow based on U and W in the symmetry plane $y = 0$ are reported in Figure 5(a). The general shape of a low-R transverse jet is observed, with an almost completely bent

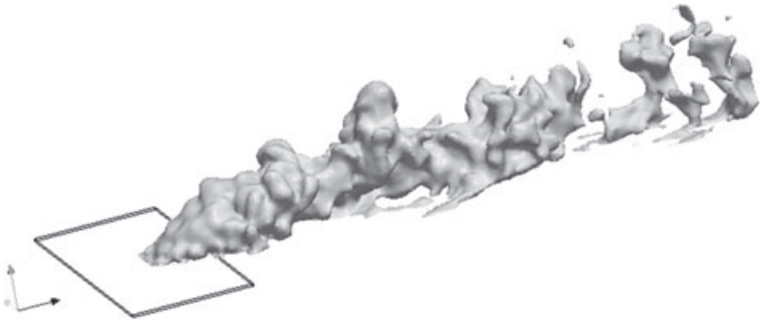

Figure 4. Scoop plate in which the heat equation is resolved and iso-surface of temperature $T = 310\,\mathrm{K}$.

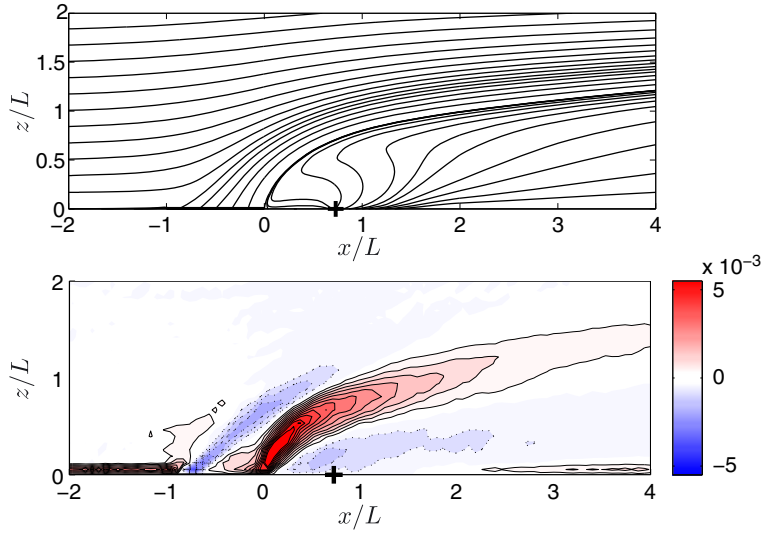

Figure 5. Mean flow structure in the the symmetry plane $y = 0$. Top: streamlines of the mean (U, W) flow; bottom: mean spanwise vorticity contours (color online). Negative levels are represented by dotted lines and positive ones appear in solid lines.

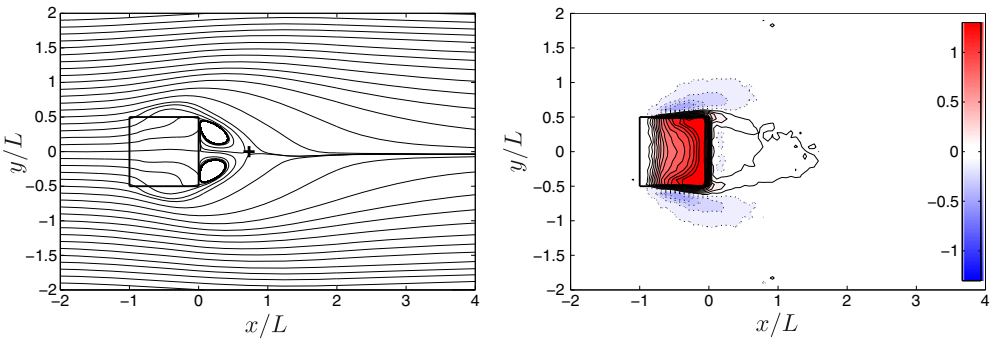

Figure 6. Mean flow structure in the $z/L = 0.066$ plane. Left: Streamlines of the mean (U, V) flow; Right: Contour of the vertical velocity component W/U_∞ (color online). Negative W levels are materialized by dotted lines and positive W levels appear in solid lines.

jet at $x/L = 2$ and $z/L = 1$. Neither horseshoe nor hovering vortex is obtained on the upstream part of the jet and no upright vortex shedding is obtained on the downstream part of it, in line with Figure (29) in [37] at $R < 2$ and a large Reynolds number ([37] observe no horseshoe vortex for $Re > 1600$). The node denoted G in Figure (24) of the same reference is recovered in the present calculations and is denoted by a cross in Figures 5(a), (b) and 6(a). It is interesting to note the similarity of the flow downstream of the jet in the present study and in [37] keeping in mind the different geometries of the jet exhaust hole.

Figure 5(b) shows that the negative y-vorticity generated on the upstream edge of the scoop hole is rapidly destroyed and that the jet has only positive y-vorticity on its upper side after $x/L \simeq 1$. This is consistent with previous observations of low-R and high-Re transverse jets [19].

The streamlines built on the (U, V) two-dimensional flow at $z/L = 0.066$ are presented in Figure 6(a). The recirculation zone downstream of the jet is well identified. Note that no averaging between the $y > 0$ and $y < 0$ parts of the domain has been made on this Figure to give an idea of the convergence of the time averaging procedure. The streamlines are only weakly deflected above the jet exit. This is because at this position the fluid keeps a significant streamwise velocity despite the proximity of the jet exhaust hole, at least above the upstream half of it. This is partly due to the low R considered here, but also and mainly due to the fact that the hot fluid from within the scoop exhausts with a nonzero streamwise velocity acquired in the scoop.

The negative W zones observed in Figure 6(b) for $0.5 < y/L < 1$ and $-1 < y/L < -0.5$ are actually due to the presence of strong $\mp x$ vorticity at $y/L = \pm 0.5$ (see Figure 7(a)). This vorticity is created by the shear due to the jet presence at $y = 0$ and the no-slip condition on the hole edges at $y/L = \pm 0.5$ and for $-1 < x/L < 0$. Figure 7(b) shows how this vorticity evolves downstream of the jet at $x/L = 0.18$, which is located in the recirculation zone downstream of the hole. As expected, the intensity of this vorticity has decreased due to viscous diffusion. The two vortices generated on the sides of the hole still do not interact at this position, and are separated by a low (V, W) velocity zone around $y = 0$ and for $z/L < 0.25$. It is interesting to note that two secondary 'anti-kidney' vortices [20] (denoted by arrows in Figure 7(b)) are present between the two counter-rotating vortices and the central low-velocity zone. Finally, Figure 7(c) presents the vorticity field downstream of the recirculation zone, with the previous major vortices even more diffused and that are interacting to form the well-known counter-rotating vortex pair (CVP) common to all JCF.

It is very clear in the present flow that the CVP is issued from the two lateral vortical regions generated by the fluid flowing through the hole at the jet base. This mechanism has been observed in previous studies on transverse jets issued from a cylindrical tube (e.g. [4]). The mechanism of CVP formation is probably even simpler to highlight in the present geometry than in the classical case of a circular-based transverse jet because the vorticity already has a strong and well identified streamwise component on the lateral sides of the square hole and because it only needs advection

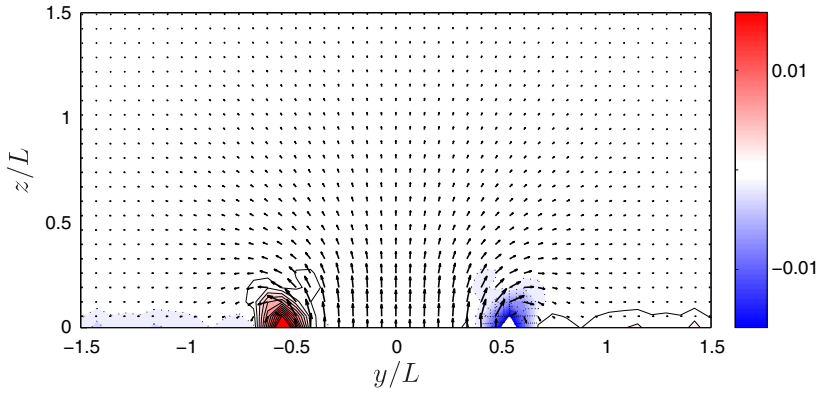

(a) $x/L = -0.5$ plane.

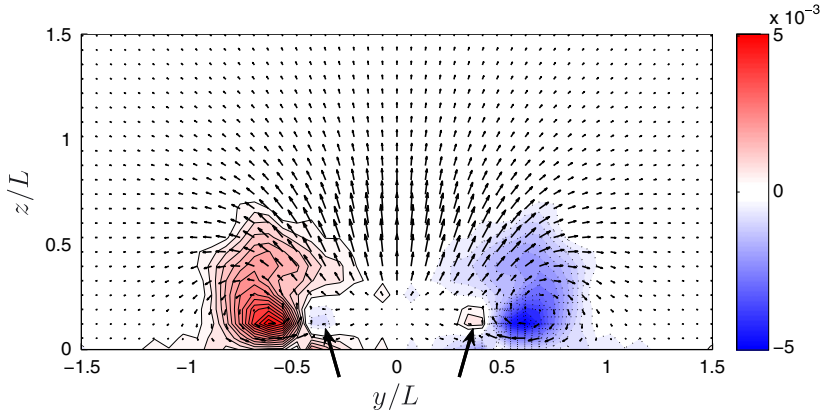

(b) $x/L = 0.18$ plane.

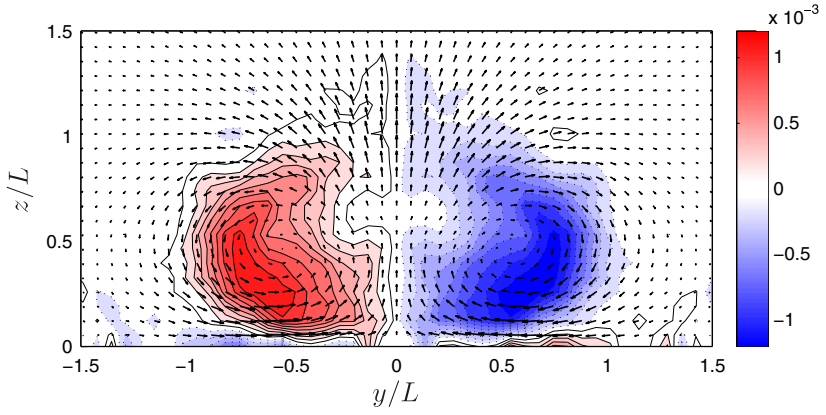

(c) $x/L = 1$ plane.

Figure 7. Mean vorticity contours (color online). Negative levels are materialized by dotted lines and positive levels appear in solid lines.

by the cross-flow to form the CVP. It is however possible that 'wall vortices' as described in [37] also feed the CVP marginally.

Note that no 'double-deck' structure is observed here [20]. This structure results from an interaction of the spanwise vorticity generated on the upstream side of the square tube feeding the jet and the cross-flow. However, in the present work, the existence of the streamwise flow in the scoop beneath the thin plate as mentioned above probably does not produce enough spanwise vorticity at

the upstream edge of the hole to form the secondary vortex pair present on the top of the transverse jet in [20].

5. COMPARISON OF LES AND EXPERIMENTAL DATA

Because there is no homogeneity direction in the present flow, the data presented here result from a time average and an average between the two symmetrical parts of the domain $y > 0$ and $y < 0$. The simulations are first initialized with a zero velocity field. During the transient period needed for the flow to adapt to the boundary conditions a robust Lax–Wendroff scheme and the dissipative Smagorinsky SGS model are used to enhance numerical stability. The transient character of the flow is controlled by monitoring the instantaneous values of velocities and temperature at several positions in the computational domain. Once a pseudo-stationary flow has developed, the numerical scheme is switched to TTGC and the SGS model is switched to either the WALE or WSM model. Then follows a second transient period of time during which the flow adapts especially to the associated reduction of numerical viscosity and diffusivity. Once this second transient is passed, the time averaging procedure is started and is conducted over 200 L/U_∞ time units.

Because the experimental data in [24] are extensively used as a reference in this section and because the document is not in English, the experimental techniques employed in that work are briefly reported here before the comparisons with the present simulations are made.

5.1. A brief overview of the experimental techniques of Albugues

Albugues [24] conducted both velocity and temperature measurements with different experimental techniques and evaluated their respective accuracy. The characteristic acquisition frequency and uncertainty associated to each technique are reported in Table II.

Concerning the velocity measurements, patricle image velocimetry (PIV) and laser Doppler anemometry (LDA) have been performed. In the LDA setup, the acquisition frequency was several tens of megahertz and hence introduced no time filtering of the signal. The tracers were 0.8 μm encens particles. Albugues [24] mentioned several possible biases in this technique (statistical, filtering, angular or gradient bias) but considered its results as very precise. In the PIV setup, 1 μm oliva oil droplets were used as particle tracers. Two LASER sources were used to obtain a small (8 μs) laps between the two successive images needed for the correlation process. Therefore, the recording frequency of the setup was linked to the maximum pulsing frequency of one laser: 10 Hz. As mentioned in [24], this frequency is too low to correctly capture the second-order moments of the velocity field. Velocity averages are expected to be correct as far as the velocity components are not too low so that the signal-to-noise ratio remains high. Indeed, Albugues estimated the error on V and W linked to their PIV device to be of order 4%–5% inside the jet (where V and W are nonzero) and of order 20% outside the jet (where both V and W tend to vanish).

Considering the temperature field, both cold-wire (CW) and infrared (IR) measurements were conducted in the bulk of the fluid and on the wall surface, respectively. The IR measurements of [24] were conducted with a high-emissivity composite material as wall. Its behaviour was supposed to be close to adiabatic, as in the present simulations. The acquisition frequency of the IR camera was 20 Hz, so that IR measurements provided only average temperature fields on the wall. [24] mentions several possible bias in the IR measurements and estimated the overall uncertainty on the temperature to be of order 0.5 K. The cold-wire technique used in [24] measures the electric resistance variations because of temperature variations of a 2.5 μm-diameter wire operated with a small constant current. The acquisition frequency of the cold wire apparatus was limited to 1 kHz due to

Table II. Limitations provided by Albugues [24] for his experimental techniques.

	PIV	LDA	Cold wire	Infrared
Acquisition frequency (Hz)	10	$O(10^6)$	10^3	20
Uncertainty	5%–20%	~ 0	n/a	~ 0.5 K

the response time of the wire. Albugues [24] does not provide a clear estimation of the uncertainty of these cold-wire temperature measurements. The only comparison is with the IR results on the wall; the cold wire measurements systematically overestimate the temperature provided by the IR technique (Figure 15 in the present article and Figure V.96 in [24]). However, note that the cold-wire measurements were conducted with an aluminium plate as wall, whereas the IR measurements were conducted with the adiabatic composite material as wall. The discrepancy between the two experimental techniques close to the wall may thus be linked to an intrinsic experimental uncertainty, but it may also be due to an overheating of the aluminium plate during the cold-wire measurements (because of the jet heating), whereas the composite adiabatic plate remained colder. The results of the cold wire technique should, in any case, be taken with caution when comparing with the present work, whereas the IR results are expected to be more reliable.

5.2. Mean velocity profiles

The U and W velocity profiles obtained from the four simulations and from the experiments in [24] on the symmetry plane and at $x/L = 1$, $x/L = 3$ and $x/L = 8$ are reported in Figure 8. The V velocity profiles have not been presented because they are roughly equal to zero both in the simulations and in the experiments for symmetry reasons.

Figure 8(f) shows that the experimental vertical velocity component does not vanish as expected, but is negative with $W_\mathrm{w}/U_\infty \simeq -0.05$. This unphysical behaviour is very likely due to the fact that the experimental device is actually a scoop mounted on a wing profile, which has a small angle of attack of 1°. Because measurements are made on the extrado of this device, the W velocity is indeed small and negative near the wall. This bias has been corrected by plotting the experimental value of $W - W_\mathrm{w}$ instead of W on Figures 8(b), 8(d) and 9(b). This is also confirmed by the fact that the experimental U/U_∞ velocity profiles where U_∞ is the free-stream velocity seemed to converge to 1.1 rather than 1 for values of $z/L \simeq 3$. Because the hot jet feels the cross-flow velocity only below a few L units above the plate, the very far-field experimental U_∞ velocity in the wind tunnel is not a relevant velocity scale. Hence, in the present work the experimental velocity profiles have been scaled by $1.1U_\infty$ so that the normalised U velocity profiles converge to 1 in the 'far' field ($z/L \simeq 4$) of the hot jet. On the velocity plots presented hereafter, an error-bar corresponding to the uncertainty W_w is added to the experimental results in [24]. This is not strictly speaking an uncertainty measure, but it provides an order of magnitude of the experimental precision that has to be expected a posteriori from the discrepancy observed in Figure 8(f). When a quantity has been measured with the two experimental techniques used in [24] (LDA and PIV), both measures are plotted and no error-bar is added for clarity.

The simulation results plotted in Figure 8 with the different SGS models and thermal boundary conditions do not differ significantly, which shows that the results concerning the average velocity field are quite robust. The agreement between LES and the experiments in [24] is good, apart for $z/L < 0.7$ in Figure 8(a). This streamwise velocity profile is taken at $x/L = 1$, a zone where an adverse pressure gradient exists due to the presence of the jet. The negative streamwise velocities measured experimentally indicate that the recirculation zone extends beyond $x/L = 1$, whereas in all the simulations the streamwise velocity component is close to zero, which means that $x/L = 1$ corresponds roughly to the end of the recirculation zone. This is confirmed by Figure 6(a). It must be recalled that the present numerical setup involves the use of wall laws at this position, and that these wall law models have generally a poor behaviour in the presence of adverse pressure gradients. Outside of this zone (namely for $z/L > 0.7$ or $x/L > 1$) the computational results agree well with the experimental data in [24].

An example of the transverse velocity field (V and W) is presented in Figure 7. A more quantitative comparison of this flow structure in the simulations and in the experiments in [24] is presented in Figure 9 where vertical profiles of V and W inside one of the vortices are shown. The agreement between the simulations and the experiment is also quantitative concerning this secondary flow structure, keeping in mind that [24] considered his LDA measurements to be more reliable than the PIV ones for low values of W/U_∞.

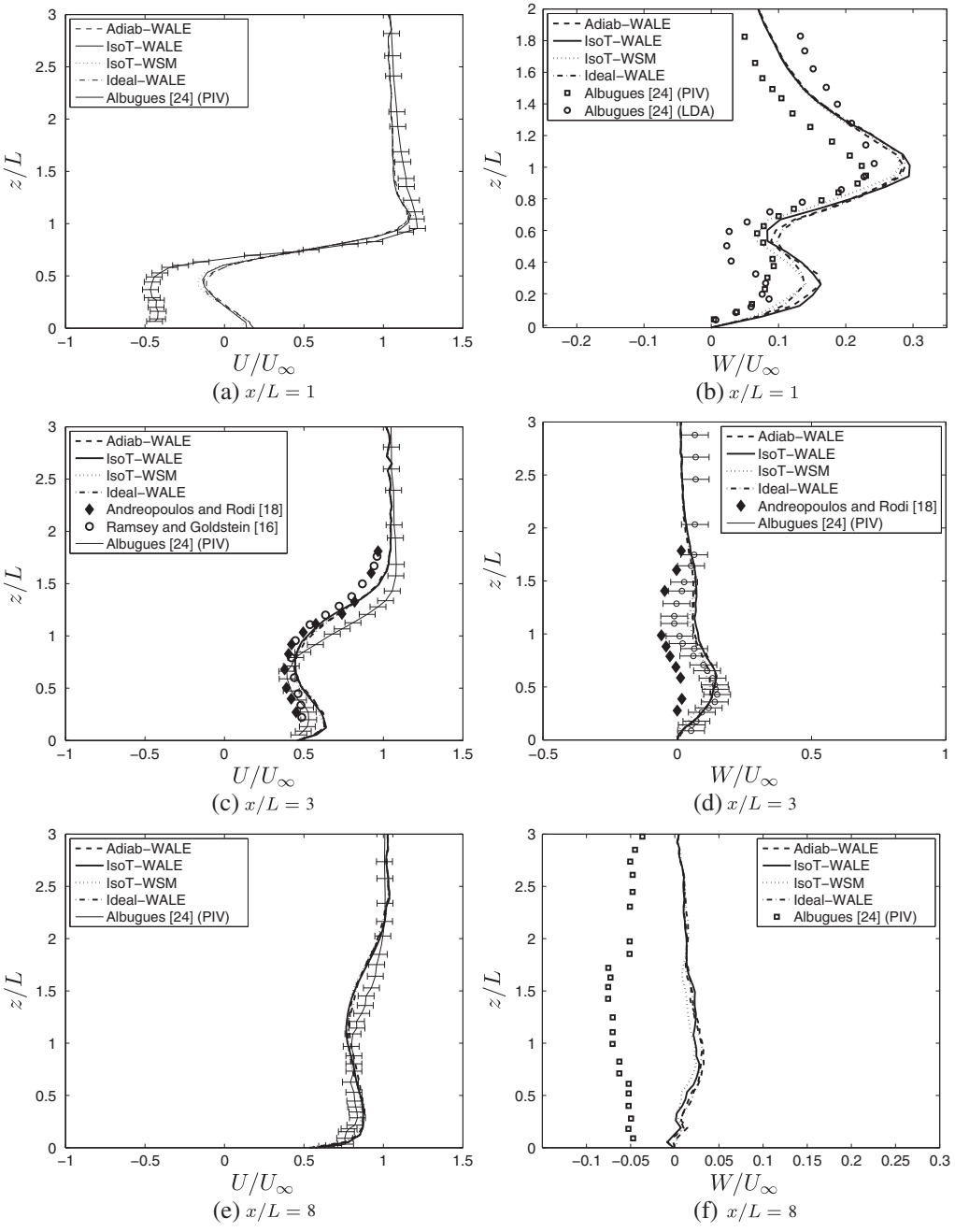

Figure 8. Nondimensional velocity profiles along the vertical z axis and at $y/L = 0$. Black diamonds: data at $x/L = 3.5$ and $R = 1$ of [18]; Open circles: data at $x/L = 2.56$ and $R = 1$ in [16] (after [18]).

5.3. Fluctuating velocity profiles

The fluctuating velocity profiles in the symmetry plane and at $X/L = 1$ are presented in Figure 10. The agreement between the simulations and the LDA experiments in [24] is quite good outside of a zone located at $z/L < 0.2$. The discrepancy close to the wall could, once again, be attributed to the use of the wall law but for a different reason. Indeed, the computation of the SGS term at the first cell is influenced numerically by the boundary condition while physically the first point is in the logarithmic region so that the Reynolds stresses at this location should be relatively independent of

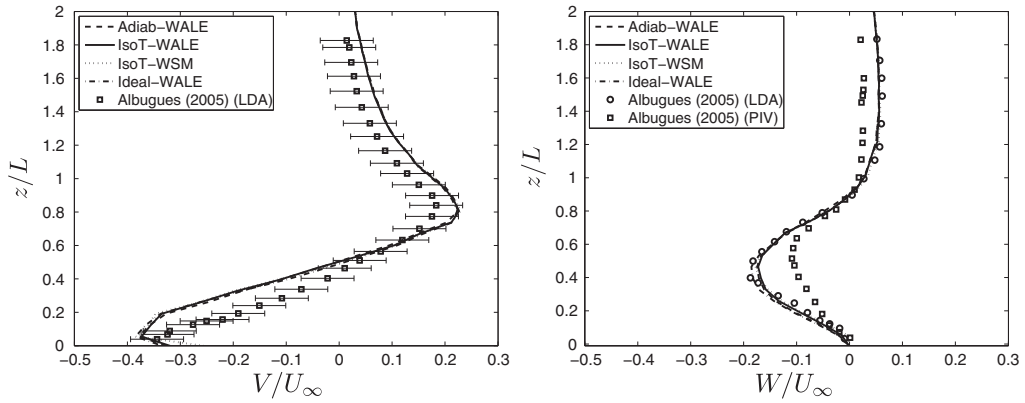

(a) $Y/L = 0.66$ (b) $Y/L = 0.83$

Figure 9. Transverse velocities V and W along the vertical z axis at $X/L = 1$.

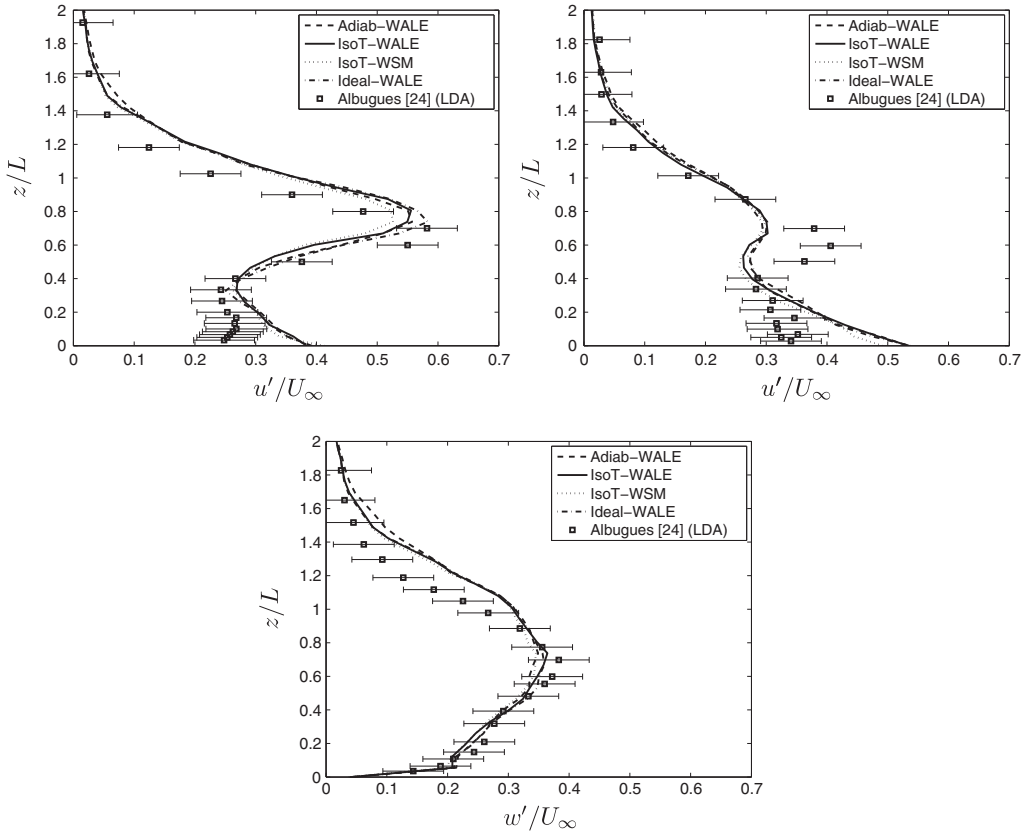

Figure 10. Fluctuating velocities along the vertical z axis in the symmetry plane and at $X/L = 1$.

the presence of the wall. This leads, in particular, to an over-prediction of the streamwise velocity fluctuations [38, 39].

Two other experimental fluctuating velocity profiles are available at $(x/L, y/L) = (1, 2/3)$ in [24] and they are compared to the numerical results in Figure 11. The fluctuating velocity levels obtained with the PIV underestimate those obtained by LDA as expected. The comparison of the present results with the LDA data in [24] shows that the numerical simulations tend to give smaller fluctuation levels. This could be expected because the LESs provide only the resolved part of the fluctuating kinetic energy.

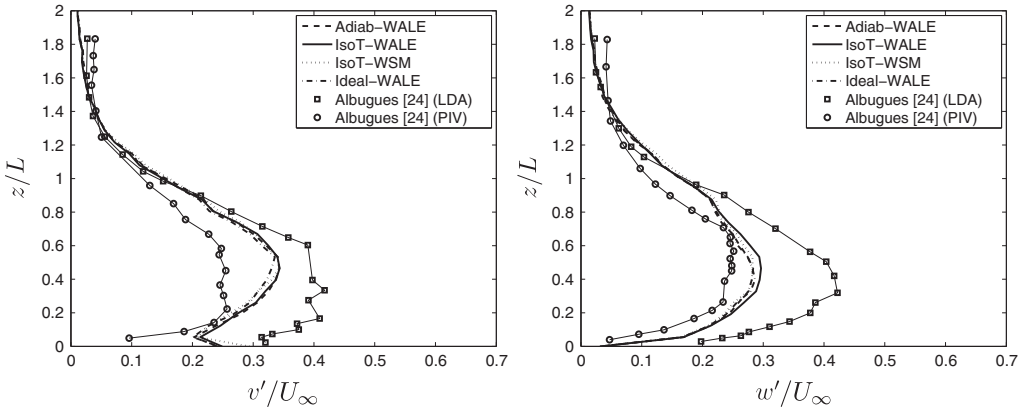

Figure 11. Fluctuating velocities along the vertical z axis at $Y/L = 0.66$ at $X/L = 1$.

No numerical configuration (boundary conditions or SGS model) distinguishes itself clearly. The enhanced WSM model did not lead to noticeable improvements of the simulations in the present work. This may be linked to the use of the wall model. Indeed, Lodato *et al*. [8] remarked that the backscatter allowed by the WSM model was especially useful in the near-wall region, which is not resolved in the present work. It must also be recognized that the simulation with the WSM model led to results identical to those with the WALE model in the jet and did not permit to improve the results at this location (see Figures 10(a) and (b)).

5.4. Wall temperature

The wall thermal efficiency decrease along the jet axis is presented in Figure 12. The results of the simulations are reported along with the experimental IR temperature measurements in [24]. The four simulations give a similar and satisfactory agreement on the wall temperature along the jet axis, but the best results are obtained using the 'ideal' boundary condition as expected (for $3 < x/L < 5$). This is due to the presence of the warm zone around the jet base in the coupled flow problem. This hot zone exists not only due to the hot air issued from jet, but also because of heat transfer through the plate in the low-velocity zone in the close wake of the jet. The improvement observed in Figure 12 for the simulation Ideal-WALE is thus directly linked to the ability to take into account precisely the coupled heat transfer in the scoop.

We now consider the wall thermal efficiency along the transverse y axis at positions $x/L = 1$ and $x/L = 8$ in Figure 13. All simulations lead to a wall thermal efficiency at $y/L \simeq 1.2$ lower than that of the experimental one. The wall temperature local minimum in the simulations at this point is

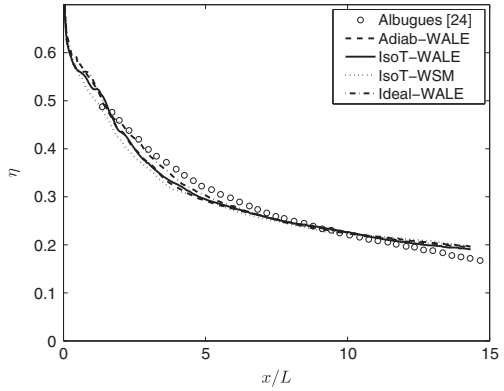

Figure 12. Wall thermal efficiency η along the jet axis x.

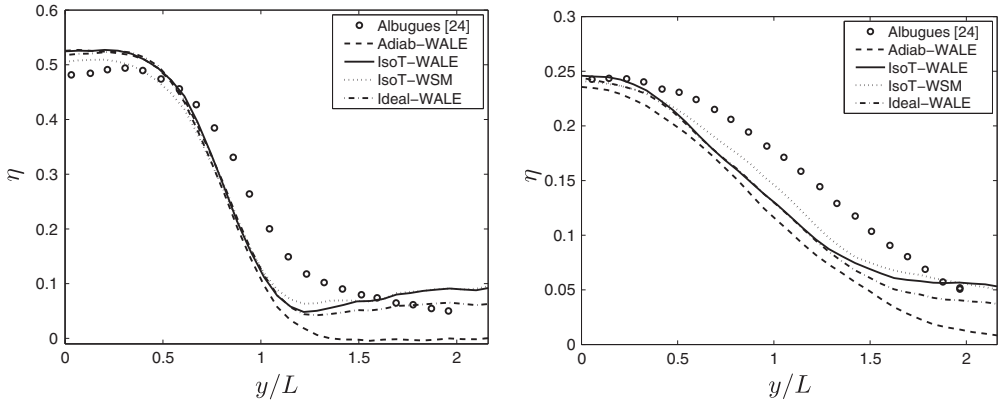

(a) $x/L = 1$ (b) $x/L = 8$

Figure 13. Wall thermal efficiency η along the transverse axis y.

consistent with the flow structure at this position; the cold exterior flow is faster on the sides of the jet above the scoop hole and is bent by the CVP so that cold air is brought to the wall on the sides of the scoop hole and slightly downstream of it. This is the white zone around the scoop hole in Figure 14(b). Hence, it is suspected that the smoother experimental wall temperature of [24] is due to unwanted thermal diffusion within the solid wall, which is impossible in the simulation because away from the scoop plate the wall is considered to be adiabatic. A coupled simulation involving the full wall (not only the scoop plate) could answer this question but would be very expensive in terms of CPU time and this slight discrepancy does not change the conclusions of (and is beyond the scope of) the present work.

Figure 13 also shows that the use of an adiabatic boundary condition leads to very poor results for $y/L > 1$. Indeed, the air issued from the scoop is heating the wall on the jet axis but not on the sides of the jet. As shown in Figure 14(b), away from the jet axis, warm air is actually present along the wall due to the thermal boundary layer developing on the top of the scoop plate, which is heated from below. The tails of the wall transverse efficiency profiles are thus directly dependent of the heat conduction through the scoop plate. Hence, if this plate is considered adiabatic as in the simulation Adiab-WALE, the efficiency away from the axis is zero as expected.

When a constant temperature is imposed on the plate as in simulations IsoT-WALE and IsoT-WSM, the thermal boundary layer can develop and leads to nonvanishing thermal efficiency for $y/L > 1$. However, the value of this efficiency is linked to the quality of the representation of the heat transfer by conduction through the scoop plate, and thus a uniform plate temperature at $T = (T_\mathrm{h} + T_\mathrm{c})/2$ is not sufficient to correctly reproduce the experimental tails in the transverse wall efficiency profiles. This explains the high values of η for $y/L > 2$ in Figure 13, for the IsoT-WALE and IsoT-WSM simulations. On the other hand, when using the coupled simulation information

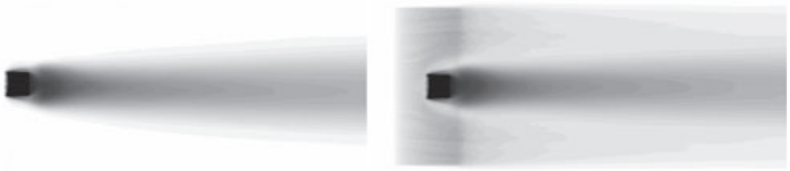

(a) Adiabatic condition (b) Isothermal condition $T = (T_c + T_h)/2$

Figure 14. Qualitative representation of the thermal efficiency η on the wall at $z = 0$ highlighting the influence of the boundary condition on the scoop plate. Black and white levels correspond to $T = 330\,\mathrm{K}$ and $T = 293\,\mathrm{K}$, respectively.

to prescribe an accurate boundary condition, the thermal efficiency level for $y/L \simeq 2$ is better predicted.

5.5. Jet temperature

The vertical thermal efficiency profiles (along the z direction) on the jet axis and at $x/L = 1$, 2.3 and 8 are presented in Figure 15. The circles denote experimental results obtained thanks to the cold-wire technique in [24], and the square on each figure is the thermal efficiency on the wall, which was obtained with the infrared measurements (experimental data presented in Figure 12). The agreement between the simulations and the experiments of [24] is quite good in the upper part of the jet for the three positions and excellent on the wall. Between the maximum efficiency location and the wall, a disagreement is found between the simulations and the cold-wire measurements. However, as mentioned in Section 5.1, the cold-wire results should be taken with caution because they do not connect to the IR measurements, which are expected to be correct within 0.5 K (or 0.01 on η) in [24]. This may be linked to a progressive heating of the aluminium wall used in [24] during the cold-wire measurements.

It is interesting to note that the four simulations give the same results not only at the wall but also above the wall. The improvement of the temperature field close to the wall observed when using the ideal thermal boundary condition is thus not recovered away from the wall and far downstream. This is due to the temperature field in the fluid is almost uniquely dependent on the advection and mixing in the jet far from the jet exhaust hole and above the wall. It is believed that in other problems where convection is less dominant, the effects of the use of a coupled thermal boundary condition should be felt more drastically.

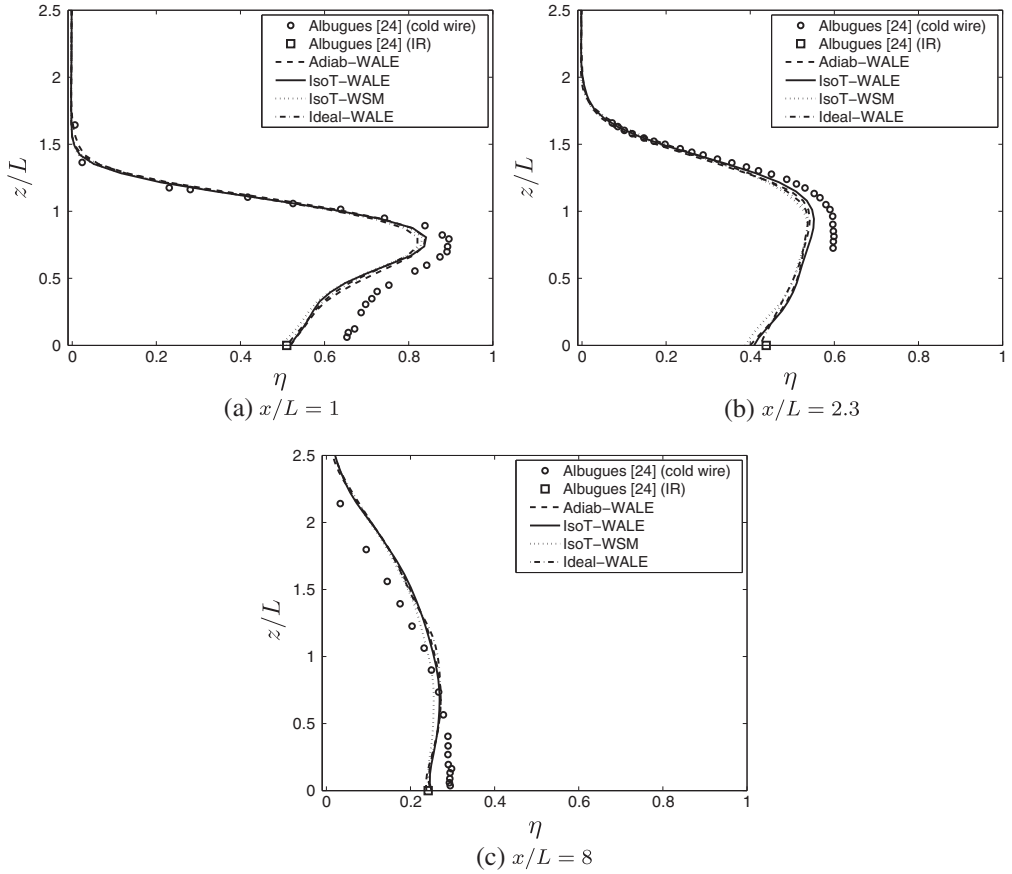

Figure 15. Thermal efficiency η along the vertical z axis.

5.6. *Fluctuating thermal efficiency profiles*

Two fluctuating thermal efficiency profiles obtained with the cold-wire technique are available in [24] and are compared to their numerical counterparts in Figure 16. One is located at $(x/L, y/L) = (2/3, 0)$ and in the z direction while the other is located at $(x/L, z/L) = (2/3, 0.57)$ and in the y direction. The discrepancy between the simulations and the experiments is quite important. Because the scalar variance is a quantity that is difficult to obtain numerically as well as experimentally, some hints are provided in the following to explain these differences.

Concerning the simulations, the constant SGS Prandtl number approach adopted here could be insufficient to recover precisely the scalar variance. Indeed, the turbulent Prandtl number (and thus Pr^{SGS}) is a quantity varying from one flow to another and even varying in space within one given flow (e.g. [40]). The idea that the poor results concerning η' is due to this modelling is supported by the good results obtained in the velocity fluctuations using the WALE subgrid viscosity. The influence of the value of Pr^{SGS} has been checked; the subgrid Prandtl number of the simulations presented in Figure 16 was 0.6 apart from the simulation Ideal-WALE in which it was set to 0.3. The simulation Ideal-WALE with $Pr^{\mathrm{SGS}} = 0.6$ led to results superimposed with those of the other simulations at $Pr^{\mathrm{SGS}} = 0.6$. The small improvement obtained by dividing the subgrid Prandtl number by a factor 2 shows that no constant subgrid Prandtl number simulation would be likely to recover the results in [24] concerning the second-order moment of the thermal efficiency. Efforts are currently under way to implement a dynamic Smagorinsky procedure to compute the SGS thermal diffusivity without hypothesis on the turbulent Prandtl number. This should lead to an improvement of the results concerning the second-order moments. However, the experimental value of the fluctuating thermal efficiency could not be recovered with a sensible value of Pr^{SGS}. Thus, a careful examination of the experimental technique employed in [24] is required.

The discrepancy between the present simulations and the measurements in [24] can also be linked to two problems in the experimental approach. First, the experimental η' profiles were obtained with the aluminium plate used as wall. As suggested in Figure 15, this plate may have overheated compared to the adiabatic wall used in the simulations. If it is true, some cold fluid entrained by the CVP close to the wall and upstream of the measurement point may have been 'preheated' by the aluminium plate before reaching the $x/L = 2.3$ location, thus reducing the amplitude of the thermal fluctuations. Another reason for an underestimated thermal fluctuation energy could be the low sampling rate of the cold-wire apparatus; it was 10^3 Hz [24] while the typical fluid velocity in the area of the cold-wire measurements in Figure 16 is at least $20\,\mathrm{ms}^{-1}$. Thus, assuming a Taylor hypothesis is roughly valid in the jet at $x/L = 2.3$ the smallest scales observable by the cold-wire measurements are of size $l = 0.02$ m, which is close to the size of the large scales of the flow ($L = 0.03$ m). To evaluate the effect of this spatial filter on the scalar variance $\langle\theta'^2\rangle = 2\int_0^\infty E_\theta(\kappa')\mathrm{d}\kappa'$, where E_θ is the scalar spectrum, it is possible to estimate the unresolved

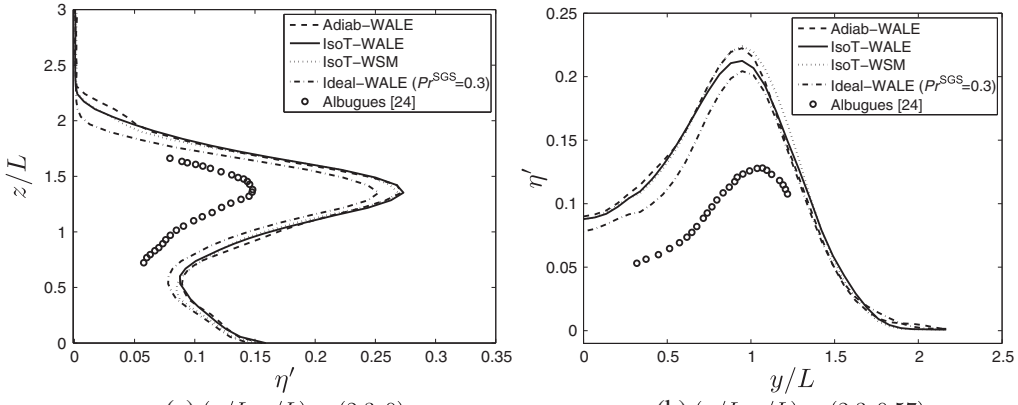

(a) $(x/L, y/L) = (2.3, 0)$ (b) $(x/L, z/L) = (2.3, 0.57)$

Figure 16. Fluctuating thermal efficiency.

part of this quantity by $\langle\theta'^2\rangle_u = 2\int_{\kappa_{CW}}^{\infty} E_\theta(\kappa')\mathrm{d}\kappa'$ where $\kappa_{CW} = 2\pi/l$. Assuming that turbulence is close to isotropy and the cutoff occurs well in the inertial-convective subrange ($Re \simeq 10^5$), the scalar spectrum can be expressed as $E_\theta(\kappa) = C_\theta \epsilon^{-1/3}\chi\kappa^{-5/3}$ where C_θ is the Obukhov–Corrsin constant, ϵ is the mean energy dissipation rate and χ is the 'dissipation' rate of the scalar variance. Then $\langle\theta'^2\rangle_u/2 = (3/2)C_\theta\epsilon^{-1/3}\chi\kappa_{CW}^{-2/3}$. This relation combined with $L = k^{3/2}/\epsilon$ and the definition of the scalar to mechanical time scale ratio $R = \langle\theta'^2\rangle\epsilon/2k\chi$ leads to the following expression for the unresolved to total scalar variance ratio:

$$\frac{\langle\theta'^2\rangle_u}{\langle\theta'^2\rangle} = \frac{3C_\theta}{2R}(2\pi L/l)^{-2/3}. \tag{4}$$

Using classical average values $C_\theta \simeq 0.5$ [41] and $R \simeq 0.5$ [42] ‡, the unresolved part of the scalar variance is found to be of order 34% of the real value. This order of magnitude analysis may explain the low fluctuating thermal efficiency reported in [24]. The fluctuating velocities did not suffer from this bias thanks to the high sampling frequency of the LDA apparatus.

6. CONCLUSION

In the present work, LESs of an aerothermal flow with conjugate heat transfer were conducted with a third-order compressible solver to evaluate the relative impact of SGS modelling and accuracy of the boundary conditions on the solution. Emphasis was put on the 'industrial' use of LES; the geometry is complex and the Reynolds number is large. Therefore, unstructured solvers have to be employed and boundary layers cannot be resolved but have to be modelled. It was chosen to reproduce numerical experiments of a JCF corresponding to the industrial application of an anti-ice system of aeronautical engine nacelles [24].

Despite the complex geometry of the jet's fluid injection system, the main features of canonical JCFs at the same Reynolds number and velocity ratio are recovered; no horseshoe, hover or upright (wake) vortex is observed, the CVP is obtained and generated as expected and even a secondary weaker vortex pair is also present.

The WALE or the WSM SGS models lead to very similar results. In the vicinity of the wall this could be expected because Lodato *et al*. [8] remarked an improvement of their results when using the WSM model especially in the buffer layer where strong backscatter exists, whereas here the boundary layer is not resolved but modelled by a wall law. An improvement of the results with the WSM model could have been expected inside the jet because Meneveau and Katz [33] and Liu *et al*. [34] highlighted the strong (resp. weak) correlation of the Leonard (resp. eddy-viscosity) tensor with the SGS stress tensor in their a priori study of a turbulent jet. However, the present a posteriori test shows that the interaction between the numerical techniques and the SGS model may not permit to obtain the expected gain, at least on this application. Another reason for the similarity of the results between the WALE and WSM simulations could be that turbulence inside the scoop is reduced when the fluid flows through the constriction constituted by scoop hole, so that the turbulence is actually developing almost only from the interaction between the jet and the cross flow. Because our results are obtained for downstream distances lower than $8L$, the flow in the jet may not be turbulent enough to rely strongly on the behaviour of the SGS model.

The choice of the thermal boundary condition on the scoop plate proved to have more influence on the flow, especially on the sides of the jet. The adiabatic boundary condition leads to a false prediction of the wall temperature on the sides of the jet. On the other hand, the uniform isothermal boundary condition on the scoop plate provides more satisfactory results because it was able to predict the nonvanishing thermal efficiency on the wall away from the jet. However, the imposed temperature value can only be chosen approximately without knowledge of the coupled heat transfer problem, which led to an overestimated heating away from the jet using the boundary condition

‡The universality and constancy of C_θ and R may be questioned (e.g. [43] and [44]) but the provided values are sufficient for the present estimation.

$T = (T_h + T_c)/2$. By computing the steady plate temperature thanks to a coupled simulation, it is possible to build an 'ideal' nonuniform isothermal boundary condition for the scoop plate. The use of this boundary condition leads to the best results. It should be added that the improvements obtained using the coupled simulation results was moderate in the present work because the constant temperature boundary condition $T = (T_h + T_c)/2$ is not very far from the real one. However, the methodology presented here is expected to bring greater refinement of the results in other systems (e.g. geometrically more complex, less dominated by advection or with larger temperature differences).

To conclude, this study shows that in LESs of industrial aerothermal flows, an accurate description of the thermal boundary conditions is as critical as the implementation of 'cutting-edge' SGS models, especially when boundary layers are not resolved. When no knowledge of the heat transfers through the walls can be obtained, conjugate heat transfer simulations can provide good estimations of the correct temperature or heat flux distributions at the walls.

ACKNOWLEDGEMENTS

We thank F. Duchaine, J. Amaya and D. Poitou for fruitful discussions and interactions concerning the numerical coupling strategies. The support of the Centre Informatique National de l'Enseignement Supérieur (CINES) which provided part of the CPU time for this project is greatly appreciated.

REFERENCES

1. Acharya S, Tyagi M, Hoda A. Flow and heat transfer predictions for film cooling. *Heat Transfer in Gas Turbine Systems (Annals of the New York Academy of Sciences)* 2001; **934**:110–125.
2. Jouhaud JC, Gicquel L, Enaux B, Esteve MJ. Large-eddy-simulation modelling for aerothermal predicitions behind a jet in crossflow. *American Institute of Aeronautics and Astronautics Journal* 2007; **45**(10):2438–2447.
3. Yuan LL, Street RL. Trajectory and entrainment of a round jet in crossow. *Physics of Fluids* 1998; **10**(9):2323–2335.
4. Yuan LL, Street RL, Ferziger JH. Large-eddy simulations of a round jet in crossflow. *Journal of Fluid Mechanics* 1999; **379**:71–104.
5. Schlüter J, Schönfeld T. LES of jets in cross flow and its application to gas turbine burners. *Flow, Turbulence and Combustion* 2000; **65**(2):177–203.
6. Smagorinsky J. General circulation experiments with the primitive equations: 1. The basic experiment. *Monthly Weather Review* 1963; **91**:99–164.
7. Nicoud F, Ducros F. Subgrid-scale stress modelling based on the square of the velocity gradient. *Flow, Turbulence and Combustion* 1999; **62**(3):183–200. DOI: 10.1023/A:1009995426001.
8. Lodato G, Vervisch V, Domingo P. A compressible wall-adapting similarity mixed model for large eddy simulation of the impinging round jet. *Physics of Fluids* 2009; **21**:035 102. DOI: 10.1063/1.3068761.
9. Margason RJ. Fifty years of jet in crossflow research, Vol. AGARD-CP-534, Winchester U (ed.), 1993; 1–41.
10. Smith SH, Mungal MG. Mixing, structure and scaling of the jet in crossflow. *Journal of Fluid Mechanics* 1998; **357**:83–122.
11. Cortelezzi L, Karagozian AR. On the formation of the counter-rotating vortex pair in transverse jets. *Journal of Fluid Mechanics* 2001; **446**:347–373.
12. Su L, Mungal M. Simultaneous measurement of scalar and velocity field evolution in turbulent crossflowing jets. *Journal of Fluid Mechanics* 2004; **513**:1–45.
13. Muppidi S, Mahesh K. Study of trajectories of jets in crossflow using direct numerical simulations. *Journal of Fluid Mechanics* 2005; **530**:81–100.
14. Muppidi S, Mahesh K. Direct numerical simulation of round turbulent jets in crossflow. *Journal of Fluid Mechanics* 2007; **574**:59–84.
15. Muppidi S, Mahesh K. Direct numerical simulation of passive scalar transport in transverse jets. *Journal of Fluid Mechanics* 2008; **598**:335–360.
16. Ramsey J, Goldstein R. An interaction of a heated jet with a deflecting stream. *Journal of Heat Transfer* 1971; **94**:365.
17. Bergeles G, Gosman AD, Launder BE. The near-field character of a jet discharged normal to a main stream. *Journal of Heat Transfer* 1976:373–378.
18. Andreopoulos J, Rodi W. Experimental investigation of jets in a crossflow. *Journal of Fluid Mechanics* 1984; **138**:93–127.
19. Andreopoulos J. On the structure of jets in a crossflow. *Journal of Fluid Mechanics* 1985; **157**:163–197.
20. Haven B, Kurosaka M. Kidney and anti-kidney vortices in crossflow jets. *Journal of Fluid Mechanics* 1997; **352**:27–64.
21. Peterson SD, Plesniak MW. Surface shear stress measurements around multiple jets in crossflow using the fringe imaging skin friction technique. *Experiments in Fluids* 2004; **37**(4):497–503.

22. Plesniak M, Cusano D. Scalar mixing in a confined rectangular jet in crossflow. *Journal of Fluid Mechanics* 2005; **524**:1–45.
23. Mendez S, Nicoud F. Large-eddy simulation of a bi-periodic turbulent flow with effusion. *Journal of Fluid Mechanics* 2008; **598**:27–65. http://www.cerfacs.fr/cfdbib/repository/TR_CFD_06_110.pdf.
24. Albugues L. Analyse expérimentale et numérique d'un jet débouchant dans un écoulement transverse. *PhD Thesis*, ENSAE - Ecole doctorale MEGeP, February 2005.
25. Lim T, Kelso R, Perry A. A study of a round jet in cross-flow at different velocity ratios. *11th Australasian Fluid Mechanics Conference University of Tasmania*, Hobart, Australia, 1992; 14–18.
26. Schønfeld T, Poinsot T. Influence of boundary conditions in LES of premixed combustion instabilities. *Annual Research Briefs.* Center for Turbulence Research, NASA Ames/Stanford Univ. 1999:73–84.
27. Moureau V, Lartigue G, Sommerer Y, Angelberger C, Colin O, Poinsot T. Numerical methods for unsteady compressible multi-component reacting flows on fixed and moving grids. *Journal of Computational Physics* 2005; **202**(2):710–736. DOI: 10.1016/j.jcp.2004.08.003.
28. Roux A, Gicquel LYM, Sommerer Y, Poinsot TJ. Large eddy simulation of mean and oscillating flow in a side-dump ramjet combustor. *Combustion and Flame* 2007; **152**(1-2):154–176.
29. Duchaine F, Mendez S, Nicoud F, Corpron A, Moureau V, Poinsot T. Conjugate heat transfer with large eddy simulation application to gas turbine components. *Comptes Rendus de l'Académie des Sciences Mécanique* 2009; **337**(6-7):550–561.
30. Duchaine F, Corpron A, Pons L, Moureau V, Nicoud F, Poinsot T. Development and assessment of a coupled strategy for conjugate heat transfer with Large Eddy Simulation. Application to a cooled turbine blade. *International Journal of Heat and Fluid Flow* 2009; **30**(6):1129–1141.
31. Colin O, Rudgyard M. Development of high-order Taylor–Galerkin schemes for unsteady calculations. *Journal of Computational Physics* 2000; **162**(2):338–371.
32. Donea J, Huerta A. *Finite Element Methods for Flow Problems*. John Wiley & Sons Inc., 2003.
33. Meneveau C, Katz J. Scale-invariance and turbulence models for large eddy simulation. *Annual Review of Fluid Mechanics* 2000; **32**:1–32.
34. Liu S, Meneveau C, Katz J. On the properties of similarity subgrid-scale models as deducted from measurements in a turbulent jet. *Journal of Fluid Mechanics* 1994; **275**:93–119.
35. Lagarde T, Piacentini A, Thual O. A. New representation of data-assimilation methods: the palm flow-charting approach. *Quarterly Journal of the Royal Meteorological Society* 2001; **127**(571):189–207.
36. Buis S, Piacentini A, Déclat D. PALM: a computational framework for assembling high performance computing applications. *Concurrency and Computation* 2005; **18**(2):231–245.
37. Kelso RM, Lim TT, Perry AE. An experimental study of round jets in cross-flow. *Journal of Fluid Mechanics* 1996; **306**:111–144.
38. Baggett J. On the feasibility of merging LES with RANS for the near-wall region of attached turbulent flows. *Annual Research Briefs,* Center for Turbulence Research, NASA Ames/Stanford Univ. 1998:267–277.
39. Cabot W, Moin P. Approximate wall boundary conditions in the large-eddy simulation of high Reynolds number flow. *Flow, Turbulence and Combustion* 2000; **63**(1-4):269–261.
40. Sagaut P. *Large Eddy Simulation for Incompressible Flows*. Springer, 2002.
41. Tennekes H, Lumley JL. *A First Course in Turbulence*. MIT Press: Cambridge, 1972.
42. Hanjalić K. One-point closure models for buoyancy-driven turbulent flows. *Annual Review of Fluid Mechanics* 2002; **34**:321–347.
43. Sreenivasan K. The passive scalar spectrum and the Obukhov-Corrsin constant. *Physics of Fluids* 1996; **8**:189–196.
44. Ristorcelli J. Passive scalar mixing: analytic study of time scale ratio, variance, and mix rate. *Physics of Fluids* 2006; **18**(075101):1–17.